Nanoscale

Accepted Manuscript

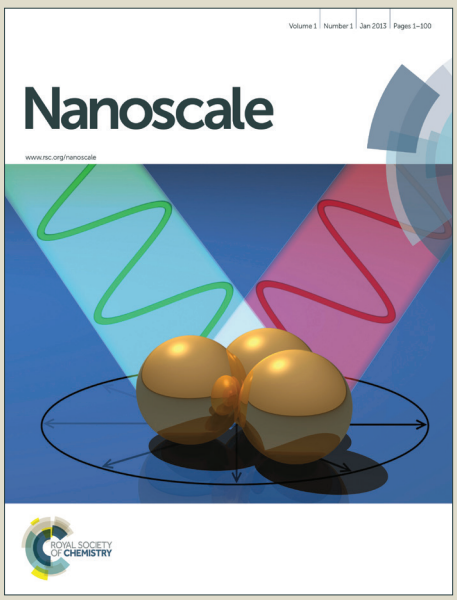

ROYAL SOCIETY OF CHEMISTRY

www.rsc.org/nanoscale

Nanoscale

RSCPublishing

COMMUNICATION

Engineering high-performance Pd core-MgO porous shell nanocatalysts via heterogeneous gas-phase synthesis

Vidyadhar Singh, [a] Cathal Cassidy, [a] Frank Abild-Pedersen, [b] Jeong-Hwan Kim, [a,#] Kengo Aranishi, [a] Sushant Kumar, [a] Chhagan Lal, [a,§] Christian Gspan, [c] Werner Grogger, [c] and Mukhles Sowwan [a,*]

We report on the design and synthesis of high performance catalytic nanoparticles with robust geometry via magnetron-sputter inert-gas condensation. Sputtering of Pd and Mg from two independent neighbouring targets enabled heterogeneous condensation and growth of nanoparticles with controlled Pd core-MgO porous shell structure. The thickness of the shell and the number of cores within each nanoparticle could be tailored by adjusting the respective sputtering powers. The nanoparticles were directly deposited on glassy carbon electrodes, and their catalytic activity towards methanol oxidation was examined by cyclic voltammetry. The measurements indicated that the catalytic activity was superior to conventional bare Pd nanoparticles. As confirmed by electron microscopy imaging and supported by density-functional theory (DFT) calculations, we attribute the improved catalytic performance primarily to inhibition of Pd cores sintering during the catalytic processes by the metal-oxide shell.

Palladium (Pd) is a well-established catalyst material,[1,2] but suffers from extremely high cost, and lifetime degradation owing to sintering and associated irreversible reduction in surface area.[3,4] To address these issues, a metal oxide shell may also prove to be a powerful tool for minimizing deactivation of the catalyst by metal sintering.[5,6] In order to achieve such improved performance via metal oxide encapsulation, a key requirement is control over the microstructure and maintenance of the high catalytic function of the core catalyst, by appropriate choice of material set and synthesis method.

In reviewing the literature on synthesis of core-shell nanoparticles, chemical methods have been widely reported.[5,7-12] Although much less common, heterogeneous gas-phase synthesis has also been reported.[13-15] For example, Xu *et al*[15] worked on the gas-phase synthesis of Co-Au and Fe-Ag core-shell nanoparticles from composite sputtering targets, with the formation mechanism being dominated by phase segregation of these immiscible materials. Independent sputtering from separate targets has also been reported for Co/Si,[16] and Ag/Au/Pd.[17] Similarly, the binary Si-Ag core-satellite and Janus nanostructures were also prepared according to our recently published procedure.[18] Using similar synthesis technique, Blackmore and co-workers recently reported on size-selected multiple-core Pt–TiO_2 nanoclusters, sputtered from single alloyed targets and also studied their catalytic activity[19]. Based on the emerging application of gas-phase synthesis to prepare binary or core-shell nanoparticles, it is evident that such a technique allows a high degree of control over critical parameters such as particle size, composition, density and electrode coverage, and it avoids the inherent products introduced by chemical synthesis from precursors and surfactants.

For catalysis applications, magnesium oxide (MgO) has frequently been studied as a support for Pd nanocatalysts.[20] For heterogeneous gas-phase nucleation of Mg and Pd, previous results on similar systems (Mg-Ti),[13,21] indicate that a Pd core surrounded by an MgO shell could be formed. Furthermore, when synthesized alone from the gas-phase, MgO nanoparticles exhibit a highly porous structure,[21] a necessary requirement in any potential catalyst encapsulant. This suggests that, via heterogeneous gas-phase synthesis, a noble metal catalyst (Pd) inside a porous metal oxide shell (MgO) might be achieved in a controllable, single step process.

With this in mind, we present a series of experiments on heterogeneous gas-phase condensation of Pd and Mg to form Pd core- Mg porous-shell nanoparticles and examine their catalytic performance towards methanol electro-oxidation.

All samples were produced using a multi-target gas-aggregated sputtering chamber (Supplementary Information, Fig. S1†).[18,22] The deposition parameters, for all experiments in the current work, are included in the Supplementary Information†. The structure of the synthesized Pd@MgO nanocatalysts is introduced in Fig. 1. The expected core-shell structure and uniformity are confirmed by transmission electron microscopy (TEM), as shown in Fig. 1a, with total diameters of approximately 10 nm. The cores are single crystalline Pd and the shells are polycrystalline MgO, with lattice spacings matching the literature values,[23,21] as shown in Fig. 1b and 1c, respectively. Inset of these figures present their corresponding TEM image simulation. Figures 1d and 1e show a HAADF-STEM (z-contrast) micrograph, and extracted EDX line profile, respectively, confirming the core-shell structure. X-ray diffraction (Figure S2†) clearly shows distinct peaks for Pd and MgO (and not any alloy phases). Further images, showing Pd and MgO deposited separately but otherwise with identical deposition parameters, are shown in the Supporting Information (Fig. S3†). These images

clearly show the porosity of the oxidized Mg structures, as reported previously. [21]

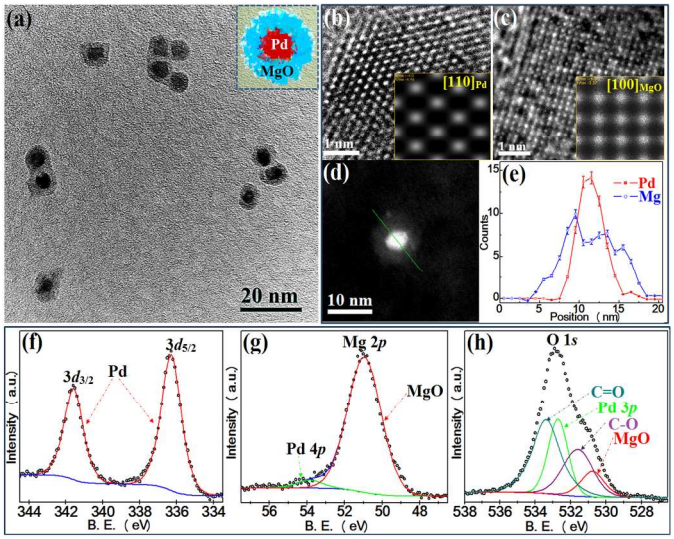

Fig. 1 (a) Low magnification TEM overview of Pd@MgO nanoparticles exhibiting core-shell morphology. (b) HRTEM image of core (Pd) region and (c) of shell (MgO) region. Inset (b), (c): simulated image of the corresponding HRTEM image. (d) HAADF-STEM image of core-shell Pd@MgO nanoparticles. (e) Distribution of Mg and Pd components in the Pd@MgO nanoparticle obtained by the line-scan analysis using STEM-EDS (along the green line in (d)). High resolution core-level XPS spectra (f) Pd 3d, (g) Mg 2p, and (h) O 1s, from Pd@MgO nanoparticles.

While TEM provides high spatial resolution on a tiny proportion of the specimen, X-ray photoelectron spectroscopy (XPS), on the other hand, allows us to gain statistical information from a wide area of the sample. A wide scan spectrum (Fig. S4†) reveals strong characteristic signals of Pd, Mg, and O (as well as C from the substrate). Figure 1f shows the XPS spectrum for the Pd 3d core level of the Pd@MgO nanoparticles. The Pd $3d_{5/2}$ peak shifts towards higher binding energy (BE), with ΔE ~0.8 eV, compared to that of Pd nanoparticles (335.5 eV). This shift in BE is due to the small amount of electron transfer from MgO to Pd, consistent with the difference in the electronegativities of Pd and Mg (Pd = 2.20 and Mg = 1.31).[24] The Pd $3d_{5/2}$ peak associated with PdO (336.7 eV) has not been observed in any of the acquired spectra.[25] Mg 2*p* core level spectra (Fig. 1g) with broad Mg 2*p* peaks revealed the presence of a certain amount of Mg-O bonds in the sample. The BE of the Mg 2*p* core level that corresponds to MgO nanoparticles (51.0 eV) is located at higher BE than for bulk metallic Mg (49.7 eV).[26] In addition, the O 1*s* spectrum is characterized by three bands (Fig. 1h): two at 532.3 and 531.6 eV, which is due to the absorption of oxygen molecules on the carbon surface, and one at 530.8 eV, which corresponds to the MgO.

Given the difference in condensation and solidification temperatures,[27,28] Pd nucleates much more quickly than Mg in a heterogeneous vapor cloud. In this situation, the pre-formed Pd clusters act as nucleation seeds for the Mg vapor, allowing rapid growth of a Mg shell on the Pd cluster, as published previously for Mg/Ti.[13] Furthermore, the surface energy of Mg (0.8 J/m^2) is significantly lower than that of Pd (2.0 J/m^2),[29] making it energetically favorable for Mg atoms to migrate or stay on the surface of the pre-formed Pd cluster, forming a shell. Finally, upon exposure to oxygen the shell oxidizes to form MgO.[21,30]

A major advantage of gas-phase synthesis is the ease with which the deposition conditions, and resultant structures, can be modified.[18] For example, the extent to which the nanoparticle size and structure could be engineered is illustrated in the STEM micrographs in Fig. 2a–2d. This was achieved simply by varying the quantity of active sputtering targets and the applied sputtering power, to the individual Mg and Pd magnetron heads (Fig. S1†). We can see four different cases, with associated size distributions, in Fig. 2e–2h. The size and internal morphology could be directly manipulated by varying the sputtering powers.

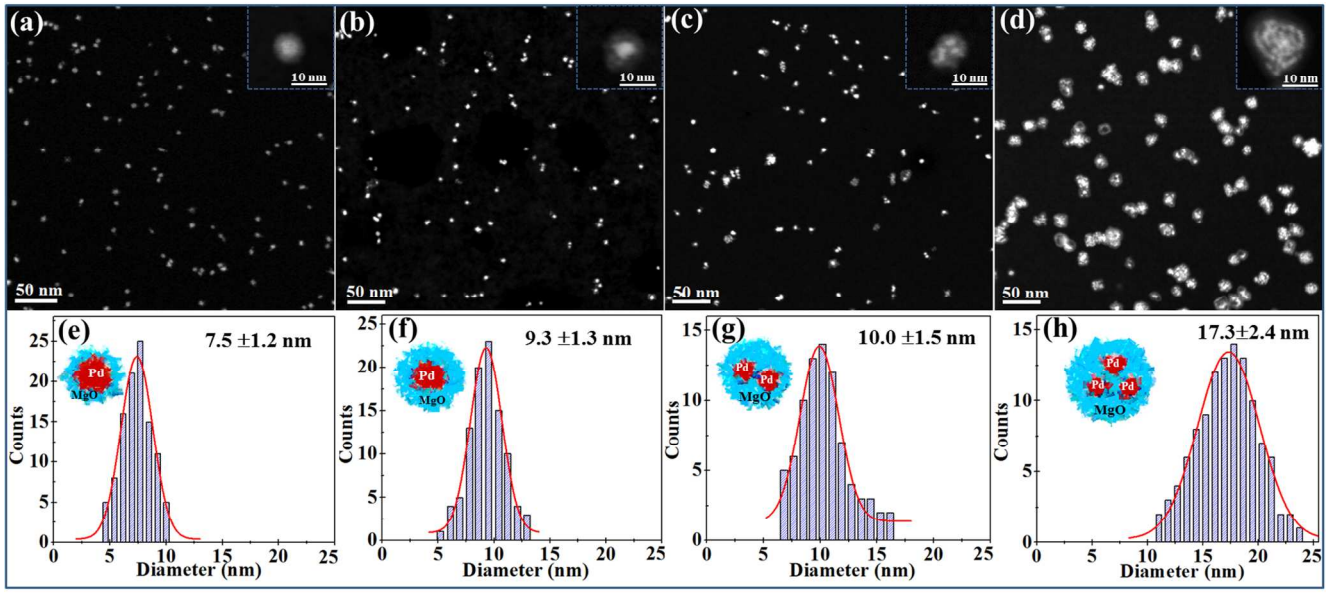

Fig. 2 Directly engineering the nanoparticle structure by varying the relative number densities of each vapor species in the aggregation zone. Low magnification STEM images (a-d) with higher magnification (inset); size distributions (e-f) of Pd@MgO nanoparticles for different Pd/Mg sputtering power ratios; (a, e) 0.66, (b, f) 0.33, (c, g) 0.14 and (d, h) 0.11.

For sputtering power ratios of 0.66, 0.33, 0.14 and 0.11, the average diameters were determined to be 7.5 ± 1.2 nm, 9.3 ± 1.3 nm, 10.0± 1.5 nm, and 17.3 ± 2.5 nm, respectively. We obtained also atomic force microscopy (AFM) height images for each of the four sputtering power ratio cases, as shown in the Supporting Information (Fig. S5†), which highlights the control of the gas-phase process.

After synthesis, the catalytic properties of these Pd@MgO core-shell structures were evaluated for electrochemical oxidation of methanol. This reaction is central to the operation of direct methanol fuel cells, whose present utilization is limited by the low efficiency of this reaction.[31] The accepted routes for the electrochemical oxidation of methanol to CO_2 consist of a direct path without an adsorbed CO intermediate, and an indirect path that involves strongly bound CO on the metal surface. The direct path involves hydroxylation at an early stage during the dehydrogenation of methanol leading to carboxyl intermediates that can form CO_2 directly without going through the CO intermediate. Because of the strong binding of CO on most monometallic surfaces the contribution from the direct path to the anode current only becomes significant when CO is removed from the surface and hence in these cases the over potential is entirely defined by the indirect pathway. The indirect path of methanol oxidation to CO_2, on the other hand, is believed to proceed via the oxidation of methanol to adsorbed CO and hydrogen, activation of water, and hydroxylation of CO leading to the final product.

$$CH_3OH \rightarrow CO + 4(H^+ + e^-)$$
$$CH_3OH + H_2O: \quad H_2O \rightarrow OH + (H^+ + e^-) \quad \rightarrow CO_2 + 6(H^+ + e^-)$$
$$CO + OH \rightarrow CO_2 + (H^+ + e^-)$$

For cyclic voltammetry (CV) measurements, nanoparticles were deposited directly onto glassy carbon (GC) electrodes,[32] as illustrated in Fig. 3a. Full details of catalyst preparation and loading are included in the Supporting Information†. For this investigation, the structures synthesized with sputtering ratio of 0.33 and size distribution of 9.3 ± 1.3 nm, as shown in Fig. 2b and 2f, were utilized. Mass current density CV curves are shown in Fig. 3b**.** Despite the low mass, good CV signals were obtained.[32] The general form of the curves is consistent with previous studies,[33] which indicates a reliable measurement environment (as does the linear variation with methanol concentration at -0.4 V, shown in Fig. 3c). Firstly, it is clear that these previously untested structures are catalytically active, demonstrating that the inert MgO shell does not passivate the internal catalytic Pd core. This in itself is a significant finding, already confirming that the MgO matrix surrounding the active catalyst did not prevent reactants from arriving and products from leaving the surface to any great extent. Furthermore, it is also immediately clear that the anodic peak current density, indicative of electrocatalytic activity, is significantly increased for the core-shell structures, in comparison to the bare Pd nanoparticles (420 μA μg^{-1} vs 120 μA μg^{-1}, respectively). The anodic onset potential for methanol oxidation reaction (MOR) also shifted in the negative direction for core-shell particles. This is shown in Fig. 3d, in which the anodic onset potentials for Pd, MgO-supported Pd, and Pd@MgO structures, are presented. To evaluate the electrocatalytic stability of the as-prepared Pd@MgO catalysts, long term chronoamperometric measurements were performed. Figure S6† shows the current-time curves measured at 0.35V for 2000 seconds. Once the steady-state has been reached, the Pd@MgO catalysts maintain a current density that is about twice as high as that of the conventional Pd/GC catalyst. Note that while rapid dissolution of MgO in acidic solutions has been reported previously, it is quite stable in alkaline solutions,[20] as utilized here.

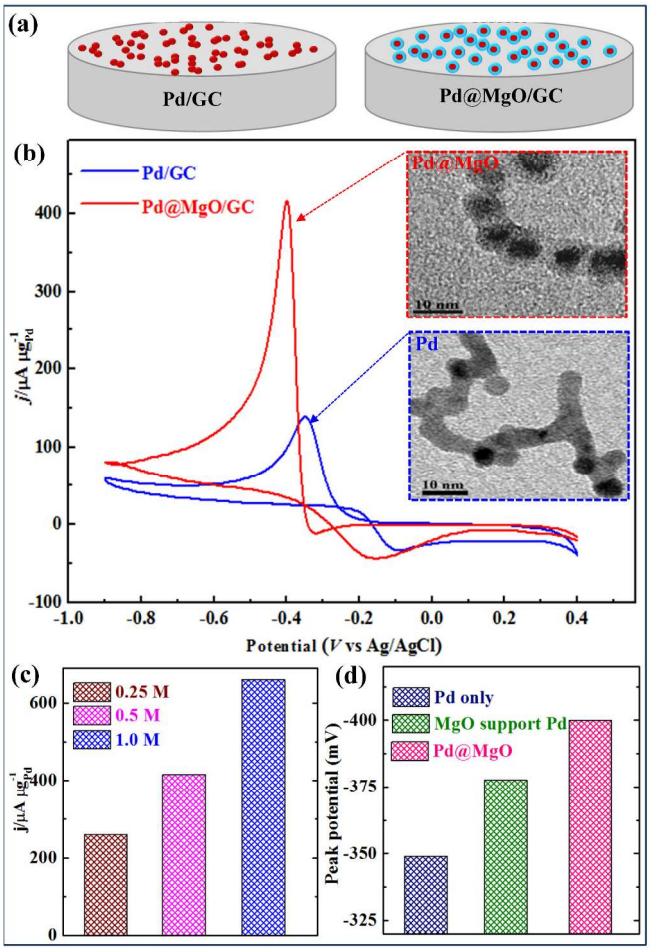

Fig. 3 (a) Schematic design of Pd and Pd@MgO catalytic nanostructures on GC electrode. (b) Cyclic voltammograms of room-temperature methanol oxidation on the Pd/GC and Pd@MgO/GC catalysts in 1 M KOH/ 0.5 M methanol at 38 mV/s. (c) Mass activity of Pd@MgO nanocatalysts for different methanol concentrations at 0.4 V (*vs.* Ag/AgCl). (d) Onset peak potential of Pd, MgO support Pd, and Pd@MgO nanocatalysts for methanol oxidation.

By considering the insets of Fig. 3b (as well as Fig. S7†), it is evident that the noble metal coalescence behavior has been significantly modified by the presence of the MgO shell. For the case of Pd alone, the originally discrete nature of the nanoparticles (as evidenced from the in-flight mass filter) has been lost to form larger agglomerations, with associated reduced surface area. We have roughly estimated the degree of coalescence and associated loss of surface area. This has been performed on a sample basis, using TEM micrographs. The in-situ quadrupole mass filter gives the original (pre-sintering) nanoparticle size distribution, immediately after nucleation, during flight from aggregation zone to substrate. As described in the Supporting Information (Fig. S8†), by identifying the substrate nanoparticles using the in-flight diameter and surface curvature, measurement of the degree of interpenetration, and by applying the modified Frenkel method,[34] the loss in surface

area is found to be significant, in the range ~35-40%. However, the coalescence behavior of Pd@MgO is quite different. While the MgO shells in many cases come into contact, they effectively act as spacers between the Pd cores. Thus, the internal Pd cores retain their original shape and do not come into contact with each other. That the catalytic activity is not inhibited by the presence of the MgO shell is directly evidenced by the strong CV signals which were obtained.

A second possible contributor to the superior performance of Pd@MgO nanoparticles which must be examined is that the reaction pathway has been modified by the presence of the MgO. To evaluate this, we have performed DFT calculations on a number of different surfaces that explicitly take the presence of Mg at the core-shell interface into account. Full simulation details are included in the Supporting Information. All total energies were calculated using Quantum Espresso and for the evaluation of exchange and correlation the BEEF-vdW functional was chosen.[35] The structure optimizations were all performed until interatomic forces reached 0.01 eV/Å with the two top most close-packed layers relaxed and the remaining layers fixed in the bulk structure. Similar for closed-shell molecules we used gas phase energies corrected with tabulated gas phase thermochemistry data all at T = 300 K. To account for the increased stabilization due to the electrolyte we have used corrections of 0.25 eV for OH, 0.15 eV for R-OH, and 0.10 eV for CO.[36] In addition, corrections to the over binding of CO estimated by DFT have also been used according to the previously reported scheme,[37] and an empirical correction of 0.41 eV for closed-shell molecules (HCOOH and CO_2) with an O-C-O backbone has been applied.[38] We constructed extended model slabs for the Pd and PdMg metal surfaces (consistently with our XPS results reported in Fig. 1). In the inserts in Fig. 4 the different surface structures used to simulate the methanol oxidation energetics are shown. For the close-packed (111) surface of Pd, a (3 × 3) slab with four atomic layers were used.

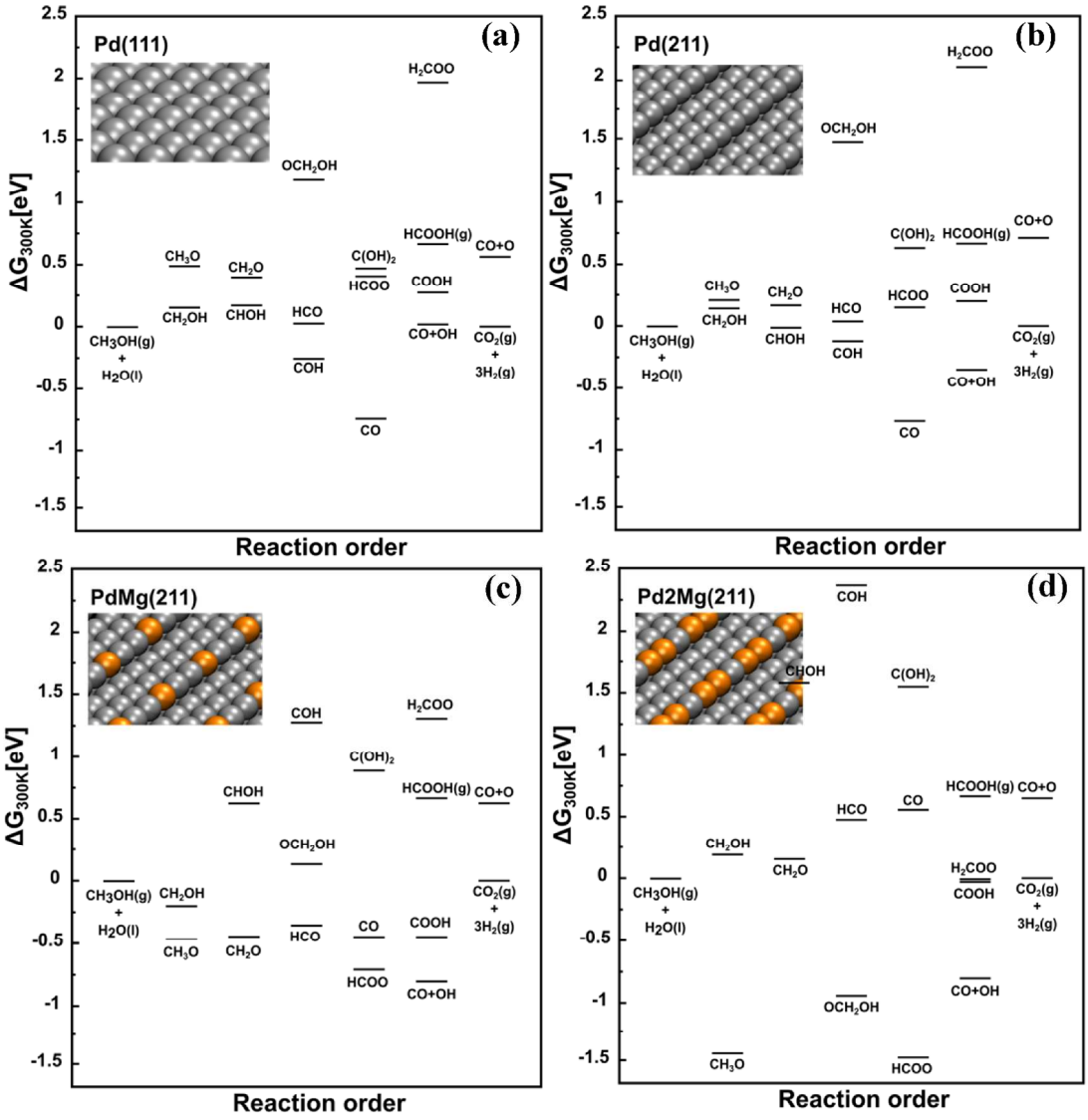

Fig. 4 Calculated adsorption free energies of all possible intermediates in the methanol oxidation reaction. The diagrams only show the most stable structures on four surfaces: (a) Pd(111), (b) Pd(211), (c) PdMg(211) and (d) Pd2Mg(211).

The adsorption energies shown in Fig. 4 have all been corrected for zero-point energy contributions, contributions due to vibrational entropy, and thermal enthalpy contributions. We have calculated the stability of all the intermediates in the direct and indirect processes on our model surfaces and, in agreement with previous studies, we find that both the close-packed and stepped pure Pd surfaces have a strongly bound CO intermediate.[39] This puts Pd in the group of monometallic surfaces where CO act as a poison for the direct pathway and the removal of CO defines the onset potential for the methanol oxidation (see Fig. 4a and 4b). The introduction of Mg at the interface introduces more favorable oxygen chemistry. In fact, the intermediates bound through oxygen are stabilized so much that methoxy or formate poisoning of these sites becomes predominant. The energetics shown in Fig. 4c and 4d does not provide evidence for an increased activity of Mg modified step sites; it rather suggests that any effect induced by Mg is an increase in oxidation occurring at the step sites, hence rendering them inactive. Furthermore, the observed shift in the onset potential is more likely to be associated with variations in the pH at the Pd surface of Pd@MgO/GC compared to the Pd/GC system. The porous media could easily induce such variations and recent studies have shown that pH changes in the environment, can lead to significant shifts in the onset potential.[40] Hence, our DFT calculations suggest that the presence of MgO is not a significant contributor to the reactivity of the Pd@MgO for methanol oxidation. This leaves the reduced Pd sintering, enabled by the MgO shell, as the dominant contributor for the increased reactivity.

Conclusions

In summary, we have developed a controlled gas-phase synthesis method for highly active noble metal-porous metal oxide core-shell nanocatalysts. Sputtering of Pd and Mg from two independent neighboring targets enabled heterogeneous gas-phase nanoparticle condensation with well-defined core-shell morphology. The catalytic properties of the Pd@MgO nanoparticles were evaluated based on the combination of experimental measurements and DFT calculations. The shell did not passivate the noble metal core, and indeed the catalytic performance was improved relative to simple Pd nanoparticles. The inhibition of Pd coalescence by the metal oxide shell was identified as the key contributor to the improved reactivity for methanol decomposition. These Pd@MgO catalysts, evaluated for methanol decomposition in this study, might also be utilized for various other reactions. The single-step, tunable core-shell structure and the superior performance of the presented nanocatalysts provides an excellent foundation to develop and optimize other noble metal-metal oxide core-shell heterogeneous nanocatalysts with tailored sizes, chemical composition, and morphologies for various catalytic reactions.

Acknowledgements

This work was supported by funding from the Okinawa Institute of Science and Technology Graduate University. F.A-P acknowledges support from the DOE Office of Basic Energy Science to the SUNCAT Center for Interface Science and Catalysis.

Notes and references

[a]Nanoparticles by Design Unit, Okinawa Institute of Science and Technology Graduate University, Onna, Okinawa, 904-0495, Japan. *E-mail: mukhles@oist.jp ; Tel: +81- (0)98-966-8622

[b]SUNCAT Center for Interface Science and Catalysis, SLAC National Accelerator Laboratory, 2575 Sand Hill Road, Menlo Park, CA, 94025, USA.

[c]Graz Centre for Electron Microscopy, 8010 Graz, Austria

[#]Current address: Graduate School of Medicine, Yokohama City University, 3-9 Fukuura, Kanazawa-ku, Yokohama, 236-0012, Japan

[§]Current address: Department of Physics, University of Rajasthan, Jaipur, Rajasthan 302004, India

† Electronic Supplementary Information (ESI) available: Experimental details, including: the synthesis of Pd@MgO nanocatalysts, characterization (AFM, GIXRD, XPS, S/TEM and electrochemistry), and DFT simulations are included in the Supplementary Information.

1. X. Chen, G. Wu, J. Chen, Xi Chen, Z. Xie and X. Wang, *J. Am. Chem. Soc.,* 2011, **133**, 3693-3695.
2. M. Perez-Lorenzo, *J. Phys. Chem. Lett.* 2012, **3**, 167-174.
3. Q. Xu, K.C. Kharas, B.J. Croley and A.K. Datye, *ChemCatChem* 2011, **3**, 1004-1014.
4. E. Antolini, *Energy Environ. Sci*., 2009, **2**, 915-931.
5. G. Li and Z. Tang, *Nanoscale*, 2014, **6**, 3995-4011.
6. J.A. Moulijn, A.E. van Diepen and F. Kapteijn, *Appl Catal. A: Gen.*, 2001, **212**, 3-16.
7. D. Ferrer, A. Torres-Castro, X. Gao, S. Sepulveda-Guzman, U. Ortiz-Mendez and M. Jose-Yacaman, *Nano Lett.,* 2007, **7**, 1701-1705.
8. Q. Zhang, I. Lee, J. B. Joo, F. Zaera and Y. Yin, *Acc. Chem. Res.* 2013, **46**, 1816-1824.
9. Z. Zhang, W. Sheng and Y. Yan, *Adv. Mater.* 2014, **26,** 3950-3955.
10. S. H. Joo, J. Y. Park, C. -K. Tsung, Y. Yamada, P. Yang and G. A. Somorjai, *Nature Mater.* 2009, **8**, 126-131.
11. Z. Yin, W. Zhou, Y. Gao, D. Ma, C. J. Kiely and X. Bao, *Chem. Eur. J*., 2012, **18**, 4887-4893.
12. H. C. Zeng, *Acc. Chem. Res*, 2013, **46**, 226-235.
13. G. Krishnan, G. Palasantzas and B. J. Kooi, *Appl. Phys. Lett.*, 2010, **97**, 261912.
14. R. E. Palmer, S. Pratontep and H.-G. Boyen, *Nature Mater.,* 2003*,* **2**, 443–448.
15. Y.-H. Xu and J.-P. Wang, *Adv. Mater.,* 2008, **20**, 994-999.
16. K. Sumiyama, T. Hihara, D. L. Peng and R. Katoh, *Sci. Tech. Adv. Mater.,* 2005, **6**, 18-26.
17. L. Martínez, M. Díaz, E. Román, M. Ruano, D. Llamosa P. and Y. Huttel, *Langmuir*, 2012, **28**, 11241-11249.
18. V. Singh, C. Cassidy, P. Grammatikopoulos, F. Djurabekova, K. Nordlund and M. Sowwan, *J. Phys. Chem. C,* 2014, **118**, 13869-13875.
19. C. E. Blackmore, N. V. Rees and R. E. Palmer, *Phys. Chem. Chem. Phys.,* 2015 (In Press) . [DOI: 10.1039/C5CP00285K]
20. F. Ringleb, M. Sterrer and H.-J. Freund, *Appl. Catal., A*, 2014, **474**, 186-193.
21. B. J. Kooi, G. Palasantzas and J. Th. M. De Hosson, *Appl. Phys. Lett*, 2006, **89**, 161914.

22. C. Cassidy, V. Singh, P. Grammatikopoulos, F. Djurabekova, K. Nordlund and M. Sowwan, *Sci. Rep.*, 2013, **3**, 5779.
23. P. Grammatikopoulos, C. Cassidy, V. Singh and M. Sowwan, *Sci. Rep.*, 2014, **4**, 5779.
24. A. L. Allred, *J. Inorg. Nucl. Chem.,* 1961, **17**, 215-221.
25. K. Paredis, L. K. Ono, F. Behafarid, Z. Zhang, J. C. Yang, A. I. Frenkel and B. R. Cuenya, *J. Am. Chem. Soc.,* 2011, **133**, 13455-13464.
26. *NIST X-ray photoelectron spectroscopic data*, NIST, USA, Web page: http://srdata.nist.gov/xps/.
27. H. Okamoto, *J. Phase Equil. Diff.* 2010, **31**, 407.
28. W. M. Haynes, *CRC Handbook of Chemistry and Physics – 95th Edition, Taylor and Francis,* (Boca Raton), 2014.
29. L. Vitos, A.V. Ruban , H.L. Skriver and J. Kollar, *Surf. Sci.,* 1998, **411**, 186-202.
30. H. Zheng, S. Wu, H. Sheng, C. Liu, Y. Liu, F. Cao, Z. Zhou, X. Zhao, D. Zhao and J. Wang, *Appl. Phys. Lett.,* 2014, **104**, 141906.
31. X. Li and A. Faghri, *J. Power Sources*, 2013, **226**, 223-240.
32. Y. Gorlin, C.–J. Chung, J. D. Benck, D. Nordlund, L. Seitz, T. Weng, D. Sokaras, B. M. Clemens and T. F. Jaramillo, *J. Am. Chem. Soc.,* 2014, **136**, 4920-4926.
33. Z. Yin, Y. Zhang, K. Chen, L. Li, W. Li, P. Tang, H. Zaho, H. Zhao, Q. Zhu, X. Bao and D. Ma, *Sci. Rep.*, 2014, **4**, 4288.
34. O. Pokluda, C. T. Bellehumeur and J. Machopoulos, *AIChE Journal*, 1997, **43**, 3253-3256.
35. J. Wellendorff, K. T. Lundgaard, A. Møgelhøj, V. Petzold, D. D. Landis, J. K. Nørskov, T. Bligaard and K. W. Jacobsen, *Phys. Rev. B*, 2012, **85**, 235149.
36. A. A. Peterson, F. Abild-Pedersen, F. Studt, J. Rossmeisl and J. K. Nørskov, *Energy Environ. Sci.*, 2010, **3**, 1311-1315.
37. F. Abild-Pedersen, M. P. Andersson, *Surf. Sci.* 2007, **601**, 1747-1753.
38. F. Studt, M. Behrens and F. Abild-Pedersen, *Catal. Lett.* 2014, **144**, 1973-1977.
39. G. A. Tritsaris, J. Rossmeisl, *J. Phys. Chem. C* 2012, **116**, 11980-11986.
40. D. Strmcnik, M. Uchimura, C. Wang, R. Subbaraman, N. Danilovic, D. van der Vliet, A. P. Paulikas, V. R. Stamenkovic and N. M. Markovic, *Nature Chem.*, 2013, **5**, 300-306.

Table of contents:

The porous MgO shell inhibited the sintering/coalescence of the Pd nanoparticles, while preserving their catalytic activity.